Ma et al. *Microsystems & Nanoengineering* (2026)12:99
https://doi.org/10.1038/s41378-026-01176-6

Microsystems & Nanoengineering
www.nature.com/micronano

ARTICLE Open Access

Microfluidic continuous flow production of noble bimetallic nanoparticles stabilized on evolvable polymer microspheres for confined synergistic catalysis

Li Ma[1], Junsheng Hou[1], Zijuan Luo[1], Xiong Zhao[1], Yilong Yao[1], Yaxuan Xiao[2], Zihan Ding[1], Zhenzhen Chen[3], Jinjia Wei[1,4] and Nanjing Hao[1,4]✉

Abstract

Microspheres with well-defined morphologies have been demonstrated as a promising catalytic carrier to modulate catalytic performance. However, the strategy for controlling the production of such microspheres with noble bimetallic nanoparticles immobilized is limited by complicated procedures and is time-consuming. Here, a facile and robust strategy is developed to prepare polystyrene (PS) microspheres with well-tailored morphology by readily altering the volume ratio of ethanol or toluene to water. Ag monometallic nanoparticles, Ag-Pt, and Ag-Au bimetallic nanoparticles were loaded on the PS matrix via a one-step continuous approach in a spiral microchannel. The hollow and open-hole structure was conducive to loading high content nanoparticles owing to its remarkable surface area, with Ag and Pt loading content are 7% and 10%, respectively. The swell-buckling theory and adsorption-reduction-infiltration mechanism were proposed to explain the PS microsphere's morphology evolution behavior and anchor noble metallic nanoparticles on PS microspheres in a spiral microchannel, respectively. The Ag-Pt@PS and Ag-Au@PS microspheres served as efficient catalysts for the reduction of 4-nitrophenol into 4-aminophenol. The effects of the support morphologies, catalyst amount, and types of noble metal nanoparticles on the catalytic performance were investigated experimentally. The results demonstrated that Ag-Pt@PS and Ag-Au@PS microspheres exhibited much superior catalytic performance than Ag@PS microspheres. More importantly, open-hole PS microspheres loaded with Ag-Pt nanoparticles exhibited the best catalytic performance, with reaction rate constant and activity parameters were $1.73 \times 10^{-2}\ s^{-1}$ and $692\ s^{-1} \cdot g^{-1}$, whereas without sacrificing catalytic activity even after five cycle reusability. The results not only provide an efficient continuous strategy for bimetallic catalysts preparation but also offer an effective strategy to regulate the noble metal nanoparticles via the support structure modulation for confined synergistic catalysis.

Introduction

Polymeric microspheres with well-defined structures have been demonstrated to exhibit unique properties and functionalities, which are of great significance for practical applications[1–3]. In recent years, hollow polymeric microspheres with tailored morphologies[4,5] have attracted considerable attention from researchers owing to their large surface area, controlled pore structure, flexible loading of desired species[6,7], and outstanding functionality[8]. Polymeric microspheres with tailored structures and large specific surface areas have been successfully applied in catalytic reactions[9,10], drug delivery[11,12], energy storage[13], and photonic crystals[14–16]. In the last two decades, numerous approaches have been proposed to prepare intelligent and morphology-controlled hollow polymeric microspheres with site-selective dissolution[17,18], including seed polymerization[19], self-templating[12], colloidal

---

Correspondence: Nanjing Hao (nanjing.hao@xjtu.edu.cn)
[1]School of Chemical Engineering and Technology, Xi'an Jiaotong University, Xi'an 710049 Shaanxi, P.R. China
[2]Key Laboratory of Education Ministry for Modern Design and Rotor-Bearing System, School of Mechanical Engineering, Xi'an Jiaotong University, Xi'an 710049 Shaanxi, P.R. China
Full list of author information is available at the end of the article

templating[5], and osmotic swelling-diffusion[7,20,21], and one-step polymerization[2]. Among the abovementioned methods, polymerization and osmotic swelling-diffusion are the most commonly used approaches to fabricate hollow polymeric microspheres. The polymerization fabrication approach is regarded as a straightforward strategy, which always requires a long time to generate a hollow structure. As for the self-templating strategy, the hollow structure is induced by the substance (like monomer, oligomer, polymer chain, or solvent) migration from the central part of the microparticle to the shell or the interface of the microsphere in the binary or the ternary system[22]. Seed polymerization refers to the pre-produced microspheres as seeds, and phase separation occurs in different substances to a distinctive extent for the hollow structure in the system. Although this approach can produce hollow microspheres on a large scale with tunable size, toxic fluid or specific organic reagents are always necessary, which poses a threat to the environment and health[22]. Apart from seed polymerization, one-step polymerization is also utilized to generate a specific hollow structure, which is limited by the defined formulations and fixed reaction conditions[18]. The approaches mentioned above always require a long time with toxic organic reagents, surfactants[23], or templates, which contradicts green and sustainable development in the chemical industry. Additionally, the prepared polystyrene microspheres with a wide size distribution, poor monodispersity[2], and collapsed or damaged morphology[24], which greatly constrain the practical applications. Therefore, developing a facile and efficient strategy to prepare morphology-controllable microspheres is of great significance for downstream sophisticated applications.

It is well acknowledged that incorporating microspheres with noble metals, like silver[9], gold[9,25], palladium[3,26], and platinum[27,28], is an efficient strategy to produce multifunctional catalyst, endowing the composite microspheres with particular physical and chemical properties and some specific functions, further extending their related applications in various fields like biomedicine, catalytic reaction[29–31], and photonic crystals[32], and dye degradation[33,34]. In recent years, noble metal nanoparticles have been involved with hollow polymeric microspheres to fabricate composite functional materials, which combine the advantages and mitigate the shortcomings of the individual hollow polymeric microspheres, with the expectation of exploring sophisticated applications. Continuous flow strategy has been demonstrated as an efficient strategy for synthesizing noble nanoparticles and effectively preventing the agglomeration of the nanoparticles[35,36]. Ag nanoparticles with good monodisperse and narrow size distribution were successfully prepared in 3 dimensions (3D) spiral microreactor and an integrated continuous flow microreactor system, respectively[35,36]. Additionally, a continuous flow strategy is anticipated to regulate the morphology of the microspheres by readily adjusting the flow rates of the fluids[37–39]. However, how to load the noble metal nanoparticles into the functional polymeric microspheres in an efficient and continuous way is still unclear. Therefore, it is of great significance to develop a continuous flow strategy to immobilize the noble metal nanoparticles into the advanced polymeric microsphere, further expanding the application potential. On the other hand, it is a well-known fact that 4-nitrophenolate (4-NP) is a highly toxic and organic pollutant existing in industrial wastewater, which is difficult to degrade, posing a serious threat to the environment and human health. In recent years, numerous published strategies, like photocatalytic degradation[40], co-catalyst catalysis[41], have been proposed to transform the 4-NP into the 4-aminophenol (4-AP) to mitigate the environmental issues[41,42]. However, the catalytic performance was greatly limited by the rarely available reaction activity sites resulting from the noble metal nanoparticles aggregation and low mass transfer efficiency induced by the low surface area[42–44]. Additionally, the activity species uniform distribution is difficult to achieve in the batch reactor, which also significantly affects the catalytic performance. Consequently, developing effective noble nanoparticles stabilized co-catalyst is expected to address this problem.

Herein, an efficient and simple strategy was proposed to synthesize the hollow, dimple- and bowl-like hollow PS microsphere with well-defined morphology and narrow size distribution in the water-ethanol system, which is free of organic swelling reagents and surfactants. A tiny amount of toluene was introduced into the system to facilitate the single hole to form on the surface of the PS microsphere. The formation mechanism of the morphology-controlled PS microsphere was proposed to explain the evolution behavior of the PS microsphere in the water-ethanol mixture with different ratios of water to ethanol. A spiral microchannel was developed to produce Ag, Ag-Au, and Ag-Pt loaded on the PS microspheres with versatile morphologies for catalytic application efficiently and controllably. The loading mechanism in the microchannel was proposed, and the fabricated composite noble-loaded PS microspheres were used for the 4-NP reduction reaction into 4-AP in the presence of $NaBH_4$. Eventually, the micro-sized composited PS microspheres were conveniently separated from the reaction system and further adopted to evaluate their reusability. This work not only develops an efficient continuous flow approach to produce noble monometallic and bimetallic nanoparticles decorated with morphology-controlled microspheres for efficient synergistic catalysis but also opens up a new pathway for the efficient, green, and sustainable management of 4-NP pollution, which converts highly toxic pollutants into valuable products with significant environmental and economic benefits.

Results and discussions

The formation mechanism of hollow PS microspheres in the water-ethanol binary system

Dispersion polymerization is a typical synthetic procedure to fabricate the PS microsphere on a micro-sized. The monodispersed PS microsphere prepared by dispersion polymerization was used as the seed to produce the hollow PS microsphere. In detail, styrene served as the monomer in the presence of the polyvinyl pyrrolidone (PVP) steric stabilizer and ammonium persulfate (APS) initiator. The water-ethanol mixture was used as the reaction medium to dissolve the styrene monomer and steric stabilizer PVP. However, this system is a non-solvent for the polymer being fabricated. Finally, the monodispersed and uniform particles were formed and distributed evenly in the reaction medium. The scanning electron microscopy (SEM) images (Fig. 1b) of the PS microspheres and the size distribution of the PS microspheres (Fig. 1a) are displayed in Fig. 1a, b. The results revealed that the fabricated PS microspheres were highly monodisperse with 1.48 μm an average size. Obviously, there was no aggregation, and the size distribution was narrow. Additionally, the transmission electron microscopy (TEM) image of the PS microsphere exhibits no apparent contrasts between the edge and the center of the PS microsphere, proving that the PS microsphere's interior structure was solid (Fig. 1c).

The fabricated PS microspheres were dispersed in water-ethanol to produce morphology-controlled hollow PS microspheres. The hollow PS microsphere was produced after PS microsphere aging for 24 h in the water-ethanol mixture (v/v = 1:5). The size distribution was displayed in Fig. 1d, which indicates that the fabricated hollow PS microsphere has a narrow size distribution. The SEM and TEM images in Fig. 1e, f revealed that a hollow structure formed in the water-ethanol mixture. The hollow PS microsphere formation mechanism is proposed as follows: once PS microspheres disperse into the water-ethanol mixture and the temperature reached up to 70 °C, the ethanol molecules were preferentially absorbed on the surface of the PS microsphere because the solubility parameters of the ethanol ($\delta_{12.7}$) and PS ($\delta_{8.9}$) are much closer compared to the solubility parameters of the water ($\delta_{12.7}$)[45]. The flexibility and mobility of the polymer increased significantly with the content of ethanol absorbed on the PS microsphere; therefore, the water molecules in the mixture were also absorbed along with the ethanol molecules. This water-ethanol then coalesced into a large domain by the surface/interfacial free energy minimization trend and generated a cavity inside the PS microsphere. The suspension was quenched in the ice bath when the PS microspheres were aged for 12 h in a water-ethanol mixture. The water domains in the PS microsphere were immobilized as a result of the low mobility of the polymer chain. Followed by the hollow structure generated after evaporating water, the hollow PS microsphere with smooth texture and uniform shell thickness was fabricated (Fig. 1f). The energy dispersive spectrometer (EDS) mapping results of the PS microsphere in Fig. 1g indicated that apart from the C, Al, and Pt elements, O and S elements were also detected, which revealed $[OSO_3]^-$ and OH^- groups may have existed on the surface of the PS microsphere. It was worth stating that the Al and Pt elements were introduced by sample preparation and conductive coating. To further clarify the surface properties of the fabricated PS seed microspheres, the zeta potential of the suspension with 0.5 wt% PS microspheres was measured, and the zeta potential value of the PS microspheres was −60.40 mV as depicted in Fig. 1h. Additionally, fourier transform infrared spectroscopy (FTIR) spectrometer was utilized to analyze the chemical groups on the surface of the PS microspheres, and the characterization results were displayed in Fig. 1i. Specifically, the stretching vibration absorption peak at 3432.27 cm^{-1} was the O-H bond, indicating the hydroxyl group was on the PS microsphere. The asymmetrical stretching vibration absorption peaks at 1028.40 and 1077.49 cm^{-1} were the S-O bond from the sulfate group, the asymmetrical flexural vibration peak at 616.84 cm^{-1}, and the symmetrical flexural vibration peak at 540.40 cm^{-1} were the S-O bond from $[OSO_3]^-$, which demonstrated that the $[OSO_3]^-$ group was present on the PS microspheres. Additionally, the stretching vibration absorption peaks at 3059.70 and 3026.27 cm^{-1} were C-H bonds of the benzene ring; the absorption peak at 2850.11 cm^{-1} was $-CH_2-$, the absorption peaks at 1450.22, 1492.56, and 1601.29 cm^{-1} were the skeleton vibration absorption peaks of the benzene ring; the absorption peak at 906.63 cm^{-1} was the C-H bond of the benzene ring, and the absorption peaks at 755.62 cm^{-1} and 698.83 cm^{-1} were the monosubstituted benzene ring. All these abovementioned characteristic peaks suggested that the fabricated PS microspheres have hydroxyl (OH–), sulfate ($[OSO_3]^-$), and benzene (–Ph) groups. A plausible mechanism for hollow PS microsphere formation was proposed and shown in Fig. 1j. Specifically, PS microspheres are inherently hydrophobic, exhibiting a stronger affinity to ethanol than to water; therefore, the ethanol molecules will preferentially penetrate the interior of the PS microspheres, resulting in the swelling of the PS microspheres (Fig. 1j(vii)). At this stage, a small number of water molecules moved into the interior of the PS

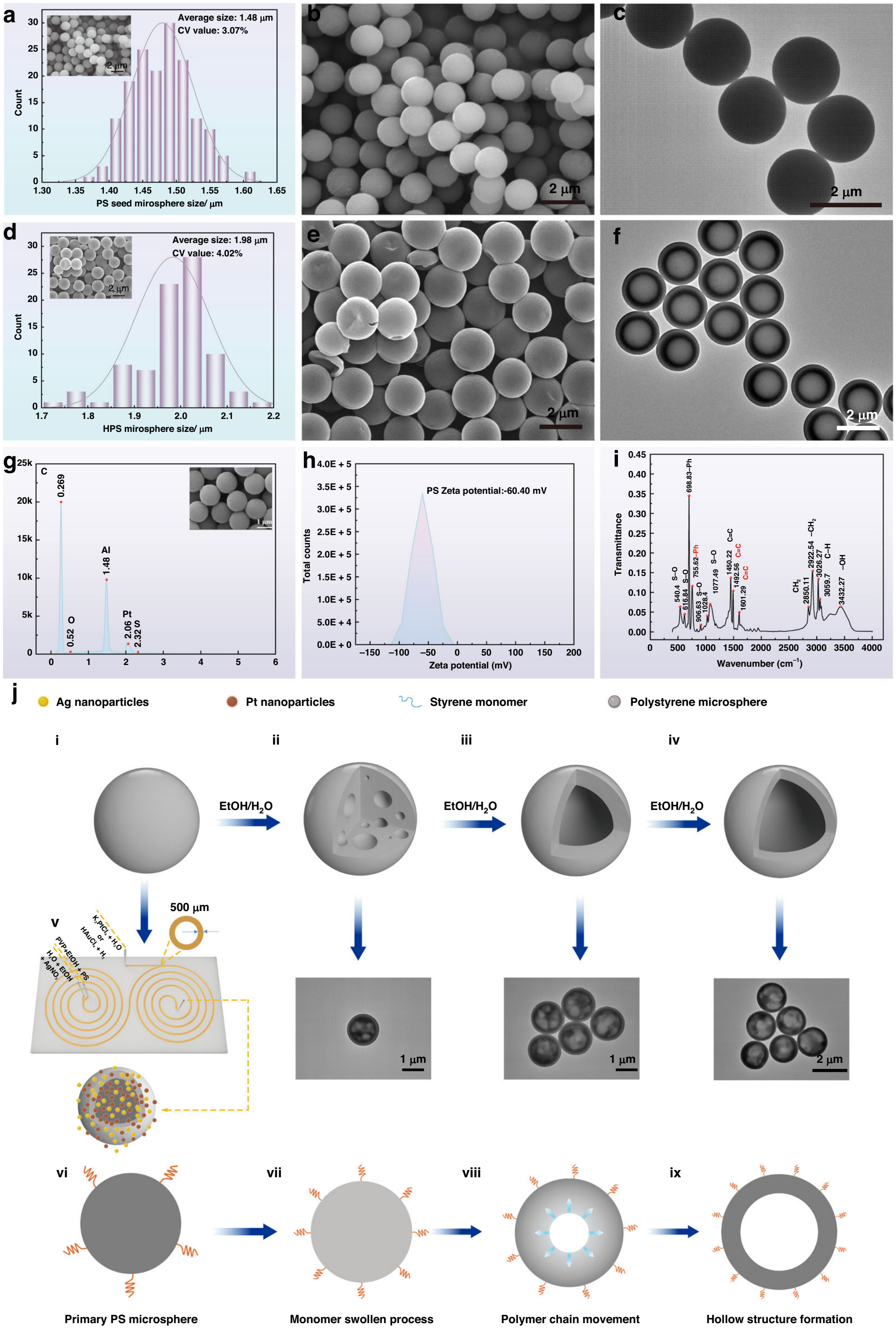

Fig. 1 The fabricated polystyrene microsphere and hollow polystyrene microsphere. **a** the size distribution of the fabricated polystyrene microsphere, **b** the SEM characterization image of the fabricated polystyrene microsphere, **c** the TEM characterization image of the fabricated polystyrene microsphere, **d** the size distribution of the hollow polystyrene microspheres, **e** the SEM characterization image of the fabricated hollow polystyrene microsphere in water-ethanol mixture, **f** the TEM characterization results of the prepared hollow polystyrene microsphere in water-ethanol, **g** the EDS mapping spectrum of the PS microsphere, **h** the zeta potential of the PS seed microsphere, **i** the FTIR spectrum of the PS microsphere, **j** the formation mechanism of hollow Ag/Pt loaded hollow polystyrene microspheres

microspheres, accompanied by ethanol molecules (Fig. 1j(ii) and Fig. 1j(iii)). Phase separation occurred with the reaction time increased between the polymer and solution phase, and polymer chains tend to migrate towards the surface of the PS microspheres and be enriched on the surface of the PS microspheres owing to the surface energy minimization (Fig. 1j(viii)). In the interior of the PS microspheres, a considerable water-ethanol solution enriched in the interior of the PS microspheres owing to the continuous movement of the polymer chain to the surface. Then, the small water-ethanol droplets coalesced and formed a large droplet, occupying the center of the microsphere and continuously growing driven by the Ostwald ripening. Eventually, the water-ethanol solution diffused, and the polymer concentration in the internal region decreased gradually, forming a cavity (Fig. 1j(iv) and (ix)).

The evolution behavior of the PS microsphere in the water-ethanol binary system

To monitor the hollow PS microsphere formation process, the solid PS microspheres were dispersed in the water-ethanol mixture, and the samples were collected at different aging time points to analyze the morphology and size of the functional hollow PS microspheres. When the volume ratio of the water and ethanol was 1:5, the overall solubility parameters is relative low, the phase separation behavior occurred on the surface of the PS microsphere, and the ethanol molecules diffuse into the interior of the PS microspheres simultaneously, the external surface of the PS microspheres initially contacted with ethanol molecules, then rapid phase separation occurred, and a thin shell formed. This phenomenon also proceeds in the interior of the PS microsphere, the internal pressure generated with the solvent evaporation. The osmotic pressure between the internal and external of the PS microspheres leading to the collapse and a shallow dimple morphology formed eventually. The results demonstrated that the cavities began to form when the aging time reached 30 min (Fig. 2a). With the reaction time continuing to increase, the size and the number of cavities increased (Fig. 2b). When the aging time reached 2 h (Fig. 2c), an evident dimple was observed on the surface of the PS microsphere, and the shell of the PS microsphere became thinner. Occasionally, there are single holes that appeared with time, and the shell became thinner and thinner (Fig. 2d–g) until some broken hollow PS microspheres appeared (Fig. 2h). The whole process of size and morphology evolution behavior in different ratios of the water to the ethanol is displayed in Figs. 2 and 3. The size of the PS microsphere increases significantly with the time increase in the water-ethanol mixture at the beginning aging stage and the solid PS microsphere gradually became hollow, and the shell became thinner and thinner. The size of the PS microsphere was increased from the initial 1.48 to 1.98 μm, as shown in Fig. 2i, and the thickness of the shell became thinner and thinner simultaneously (Figs. 1j(iii), (iv), (viii) and (ix)). At the initial 6 h, the size of the PS microsphere increased gradually because the cavities were formed in the interior of the solid PS microsphere. However, the size of the functional hollow PS microsphere remains constant when the aging time reaches 10 h, when the aging time exceeds 12 h, a considerable number of hollow PS microspheres were broken, as shown in Fig. 2h. It is worth noting that dimple- and bowl-like hollow microspheres also could be produced by adjusting the aging time and the composition of the water-ethanol mixture.

When the volume ratio of the water to ethanol was set as 1:7.5, the PS microsphere exhibited a clear dimple morphology, and with reaction time increased, the dimple morphology gradually became bowl-like morphology with time increased, as illustrated in Fig. 3a, b, the insert image displayed the TEM images of the dimple and bowl-like microspheres with the reaction time increased. To investigate the effect of the composition of the mixture on the evolution behavior of the PS microsphere, we adjust the volume ratio of the water to ethanol to 1:8, to observe the evolution behavior of the hollow PS microsphere, the SEM images of the PS microsphere are displayed in Fig. S1. It was apparent that the morphology of the PS microsphere is significantly different from the evolution behavior of the PS microsphere in the water-ethanol (1:5) mixture. Apart from regular morphology evolution, patchy, peanut-like, and triangular hollow microspheres were fabricated in the water-ethanol (1:8) mixture induced by the temperature-regulated swelling-deswelling and colloid microsphere self-assembly. On the contrary, polymeric microspheres with these controlled morphologies always required additional procedures or specific swollen reagent involvement.

To further figure out the evolution mechanism of the dimple PS microsphere in a water-ethanol mixture system (v/v = 1:7.5), the milky white sample was collected at different reaction times to evaporate the solvent and monitor the morphology evolution behavior of the PS microsphere by SEM, as demonstrated in Fig. 3a, b. The morphology evolution mechanism could be explained by Fig. 3e(i, ii), which increased the ethanol volume ratio from 83.3% to 88.2%, the high concentration of ethanol leading to the drastic dissolution, even facilitating the polymer chain to dissolve. The ethanol molecule continuously migrates from the surrounding environment into the interior of the PS microspheres, leading to an obvious concentration gradient from the interior to the exterior of the PS microspheres. With reaction time increased, ethanol and water molecules gradually diffuse from the interior, accompanied by the polymer chain

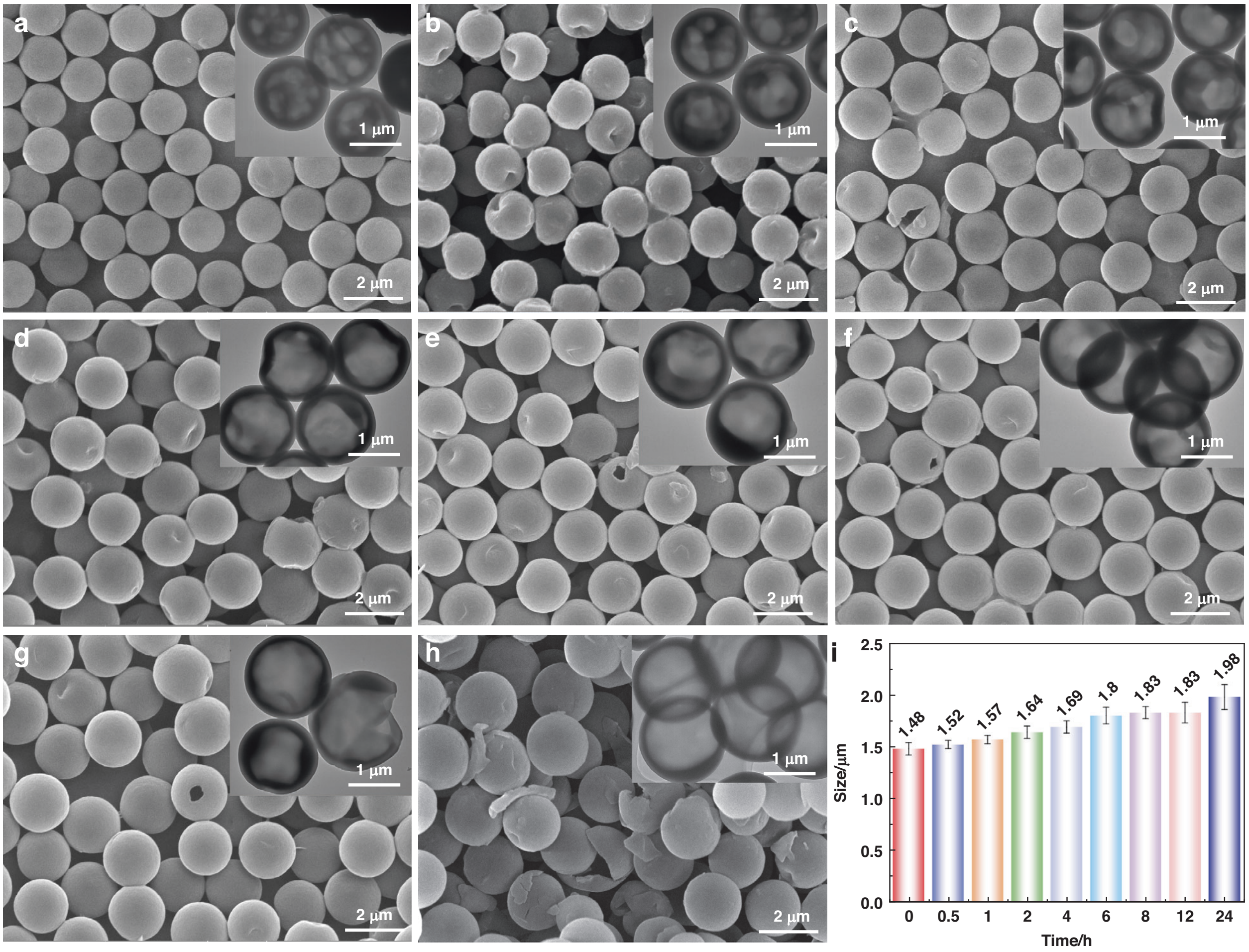

Fig. 2 The evolution behavior of hollow polystyrene microspheres in the water-ethanol mixture (water: ethanol (v:v) = 1:5). **a** 30 min, **b** 1 h, **c** 2 h, **d** 4 h, **e** 6 h, **f** 8 h, **g** 12 h, **h** 24 h, **i** the effect of the reaction time on the hollow PS microsphere size

collapsing and aggregation owing to the reduction of the internal solvent, leading to the overall shrinkage of the PS microspheres. The uneven shrinkage degree between the interior and exterior causes tensile stress. Then, the internal shrinkage stresses need to be released by deformation and gradually evolve into the obvious dimple, however, the dimple morphology is metastable, with time increased, the system tends to an equilibrium state driven by the minimized interfacial energy, which facilitates the transition of the metastable dimple morphology to thermodynamically stable bowl-like morphology, as illustrated in Fig. 3e(i, ii). All these results indicated that the strategy proposed in this study is facile, robust, and efficient, and we compared the presented synthetic approach with published strategies for morphology-controlled polymeric microspheres preparation in Table S1. Additionally, a tiny amount of toluene (8.26 v%) was introduced into the PS aqueous solution to further study the evolution behavior of the dimple PS microspheres. The results indicated that the unsymmetrical dimple morphology gradually evolved into open-hole morphology within 5 min (Fig. 3c−e). The morphology evolution behavior could be explained by the following mechanism: at the initial stage, the capillary force at the concave surface tends to absorb toluene molecules based on the Young-Laplace equation, causing a relatively high concentration in the concave zone, which further leads to a high degree of polystyrene swelling and corresponding low viscosity good mobility. The stress concentrates in the zone and enables the dimple zone rupture in priority, forming an open cavity leading to the interior.

One-step synthesis of Ag/Pt-immobilized functional PS microspheres in a spiral microreactor

The noble metal nanoparticles loaded with hollow polymer microspheres are expected to endow the functional polymer hollow microspheres with additional unique properties and extend their related applications.

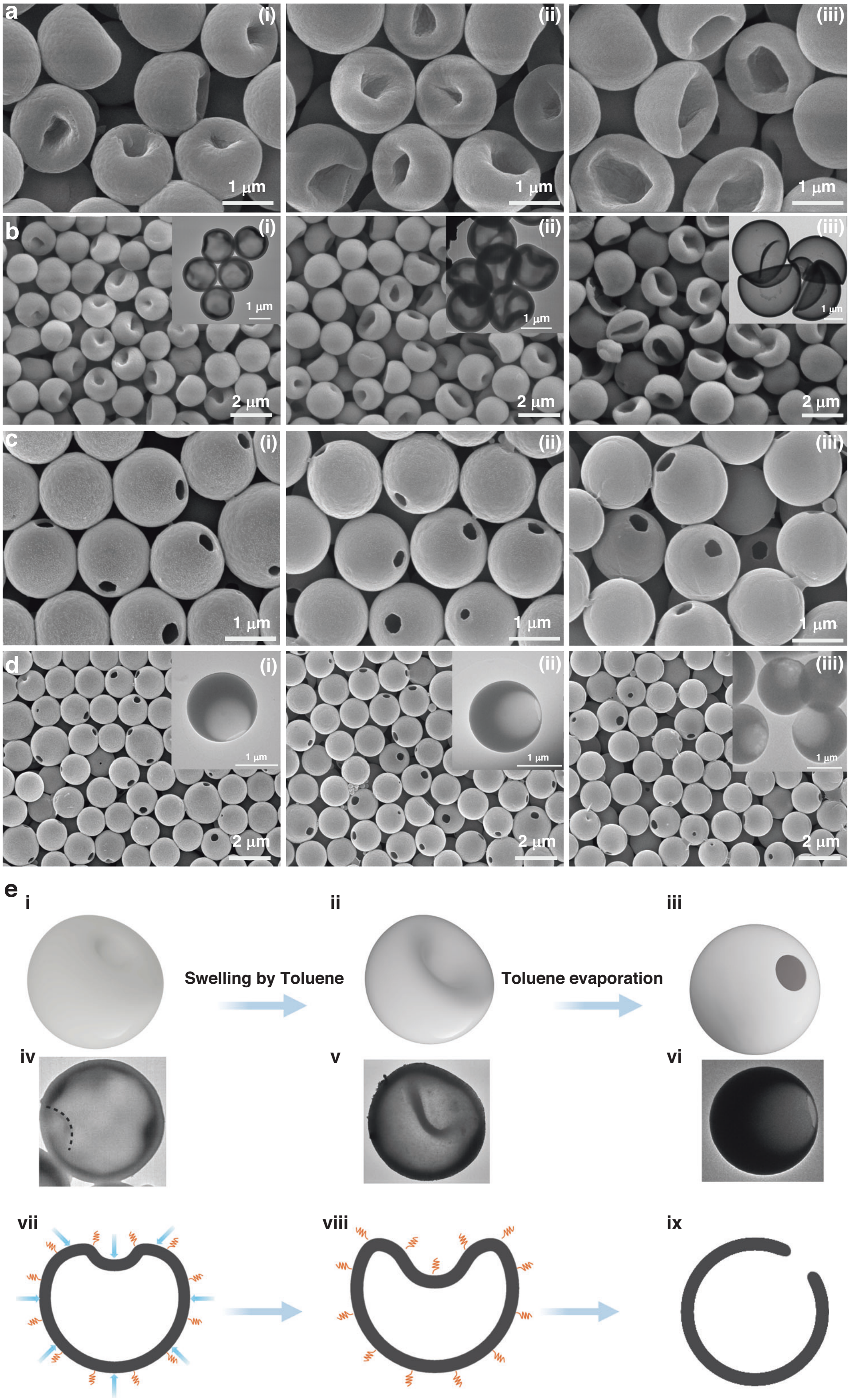

Fig. 3 The evolution behavior of hollow polystyrene microspheres in the water-ethanol (a ~ b) and water-toluene (c ~ d) mixture (water: ethanol (v:v) = 1:7.5; water: toluene(v:v) = 10:1). **a** SEM images at 50 Kx with reaction time at 30 min, 1 h, and 3 h, respectively, **b** SEM images at 20 Kx with reaction time at 30 min, 1 h, and 3 h, respectively, **c** SEM images at 50 Kx magnification with reaction time at 3, 5, and 10 min, respectively, **d** SEM images at 20 Kx magnification with reaction time at 3, 5, and 10 min, respectively, **e** the evolution mechanism of the PS microspheres in water-ethanol and water-toluene mixture

The published research has demonstrated that the PS microsphere exhibits excellent stability in the water-ethanol mixture medium owing to the electrostatic repulsion forces induced by the sulfate groups on the surface of the PS microsphere [20]. However, the PS microsphere will also aggregate in the presence of the Ag ion because the ion will significantly prevent the electrostatic stabilization. A 250 mL round bottle flask was used to prepare Ag-embedded PS microspheres, the synthetic procedures are described in Note S1, and the SEM and TEM images of the Ag@PS at different times were displayed in Fig. S2. From the SEM and TEM images, a small amount of Ag nanoparticles was immobilized on the PS microspheres, and the PS microspheres keep a solid structure even after 12 h, the solid PS microsphere with limited surface area and a small amount of Ag nanoparticles loading, which is not beneficial for the downstream catalytic applications. Therefore, we adopted a one-step continuous flow synthesis strategy to load Ag nanocrystals in the process of the hollow microspheres formation in a spiral microchannel, as demonstrated in Fig. 4a−c. Specifically, PS seed and PVP were dissolved in ethanol served as one fluid, and $AgNO_3$ was dissolved in water-ethanol mixture served as another fluid, the fluids were transported into the spiral microreactor by the syringe pump (Havard pump, 33 DDS) and the overall residence time of the fluid in the microchannel and polytetrafluoroethylene tube was calculated as approximate 5 min, and the flow regime was also determined as laminar flow according to the Reynolds number. Finally, the product was collected into a 20 mL vial, which placed at an electric heating platform at 70 °C. The reaction mixture continuously executed reaction approximately 5 min in 70 °C water bath, the prepared Ag@PS product show in Fig. 4i. The size of the Ag nanoparticles was 20–30 nm, and the size distribution measured by the zeta instrument was depicted in Fig. S3f. The SEM image of Ag nanocrystals at different magnifications was displayed in Fig. S3a–c. The SEM image (Fig. 4d) and TEM characterization results (Fig. 4e, f) indicated that the Ag nanocrystals were also successfully embedded into the PS microsphere in situ in the spiral microchannel within 10 min, which greatly simplifies the hollow PS formation and noble metal modification process. Moreover, high resolution transmission electron microscopy (HRTEM) results (Fig. 4g, h) observed that the fringe lattice of the Ag nanoparticles is 0.23 nm, proving that the Ag nanoparticles have been successfully loaded on the hollow microsphere. Moreover, the EDS mapping characterization results demonstrated that the Ag nanoparticles were distributed evenly on the PS microsphere (Fig. 4j). Compared with the traditional synthetic strategy, it was obvious that the continuous flow strategy not only greatly shortened the loading time from tens of hours to several minutes but also effectively prevented the aggregation of the Ag nanoparticles. More importantly, the hollow structure of the Ag@PS endows microspheres with a large surface area and allows them to absorb more Ag nanoparticles, which facilitates the efficient mass transfer and improves the catalytic reaction.

Compared to the standard PS microspheres, hollow, open-hole PS microspheres are expected to have a larger specific surface area and specific confined microenvironment. Monometallic and bimetallic hollow and single open hole hollow PS microsphere were also successfully prepared in a continuous spiral microreactor by changing the PS seeds, as demonstrated in Fig. 5b–d, which is expected to provide both a large surface area and a specific microenvironment for synergistic catalytic reaction and anticipated to improve catalytic efficiency.

The following plausible mechanism was proposed to explain the Ag-loading behavior, because the APS served as the radical initiator in the synthesis of PS microspheres; therefore, a large amount of sulfate groups was generated and induced by the APS decomposition reaction in the system. The produced persulfate group was absorbed onto the surface PS microsphere. When the metal precursor $AgNO_3$ was introduced into the system, Ag^+ could diffuse into the mixture and was attracted by the sulfate group on the surface of the PS microspheres by electrostatic attraction effect[46,47], and then Ag^+ reacted with the OH^- as expressed in Eq. (1) and depicted in Fig. 5a(ii).

$$2Ag^+ + 2OH^- \rightarrow Ag_2O + H_2O \tag{1}$$

It was noticeable that the Ag_2O is extremely unstable in the water-ethanol mixture, followed by the reduction reaction with ethanol in the reaction mixture. Then, it formed Ag nanoparticles gradually, as described in Eq. (2) and Fig. 5a(iii).

$$2Ag_2O + CH_3CH_2OH \rightarrow 4Ag + CH_3COOH + H_2O \tag{2}$$

To further improve catalytic performance, except that the monometallic Ag nanoparticles were successfully embedded on the PS microsphere within 10 min, K_2PtCl_4 and $AgNO_3$ aqueous solutions were simultaneously introduced into the spiral microreactor (Fig. 6a) to produce bimetallic Ag and Pt nanoparticle-embedded PS microspheres to improve catalytic reaction performance. The K_2PtCl_4 and $AgNO_3$ aqueous solution were mixed sufficiently in the microchannel, and rapid formed Ag and Pt nanoparticles owing to its extraordinary mass transfer efficiency at the microscale, and the formed Ag and Pt nanoparticles were quickly adsorbed on the morphology-

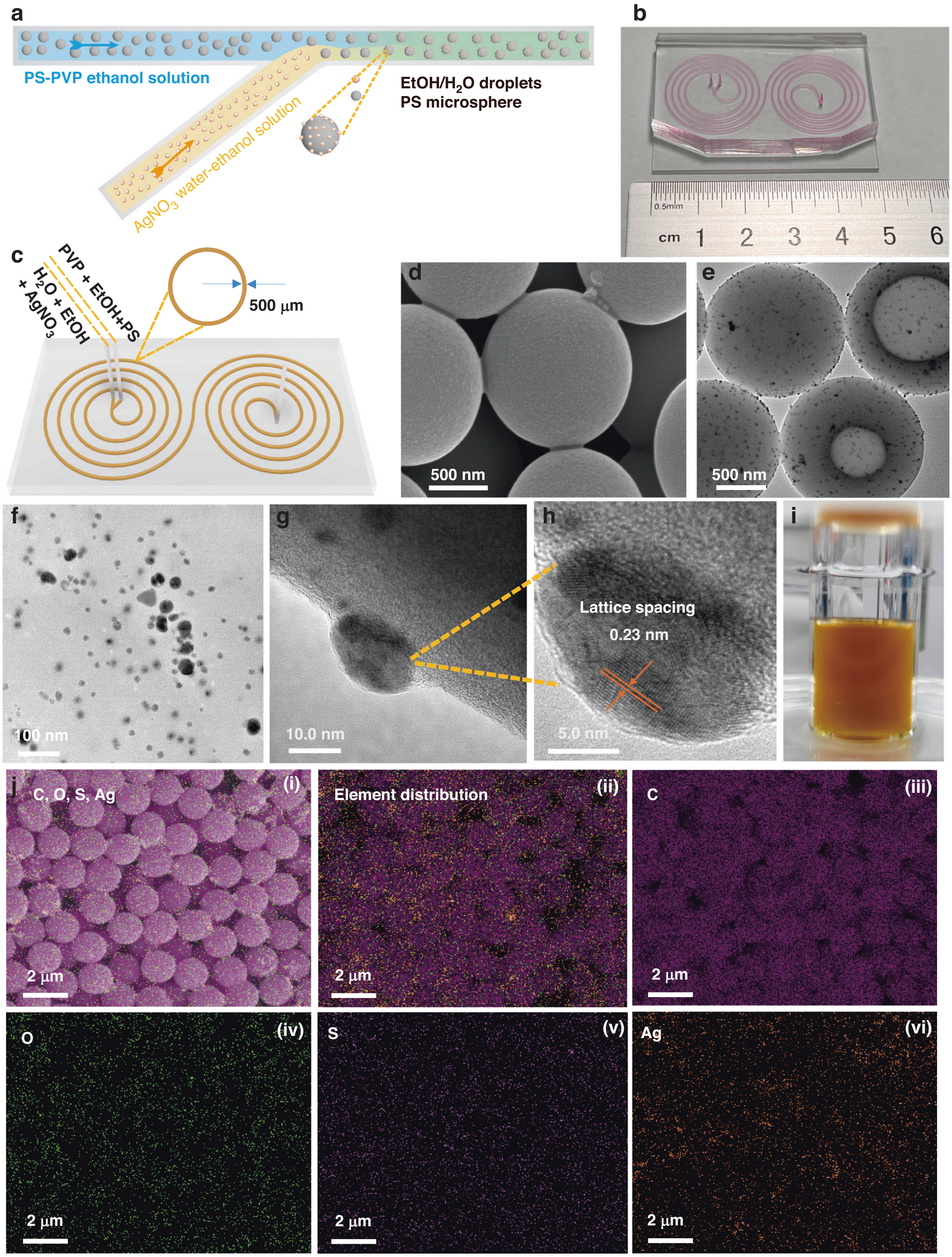

Fig. 4 Continuous flow synthesis of Ag@PS microspheres in a spiral microreactor. a the Ag@PS microsphere formation mechanism in the spiral microreactor, **b** the physical diagram of the PDMS spiral microreactor, **c** the schematic diagram and the geometrical parameters of the spiral microreactor, **d** SEM image of the Ag@PS microsphere fabricated in the microreactor, **e** TEM image of the Ag@PS microsphere, **f** the TEM image of Ag nanoparticles distribution on the PS microsphere, **g**, **h** HRTEM of the Ag nanoparticle and fringe lattice, **i** the product of the Ag@PS microsphere produced in the spiral microreactor, **j** EDS mapping of Ag@PS

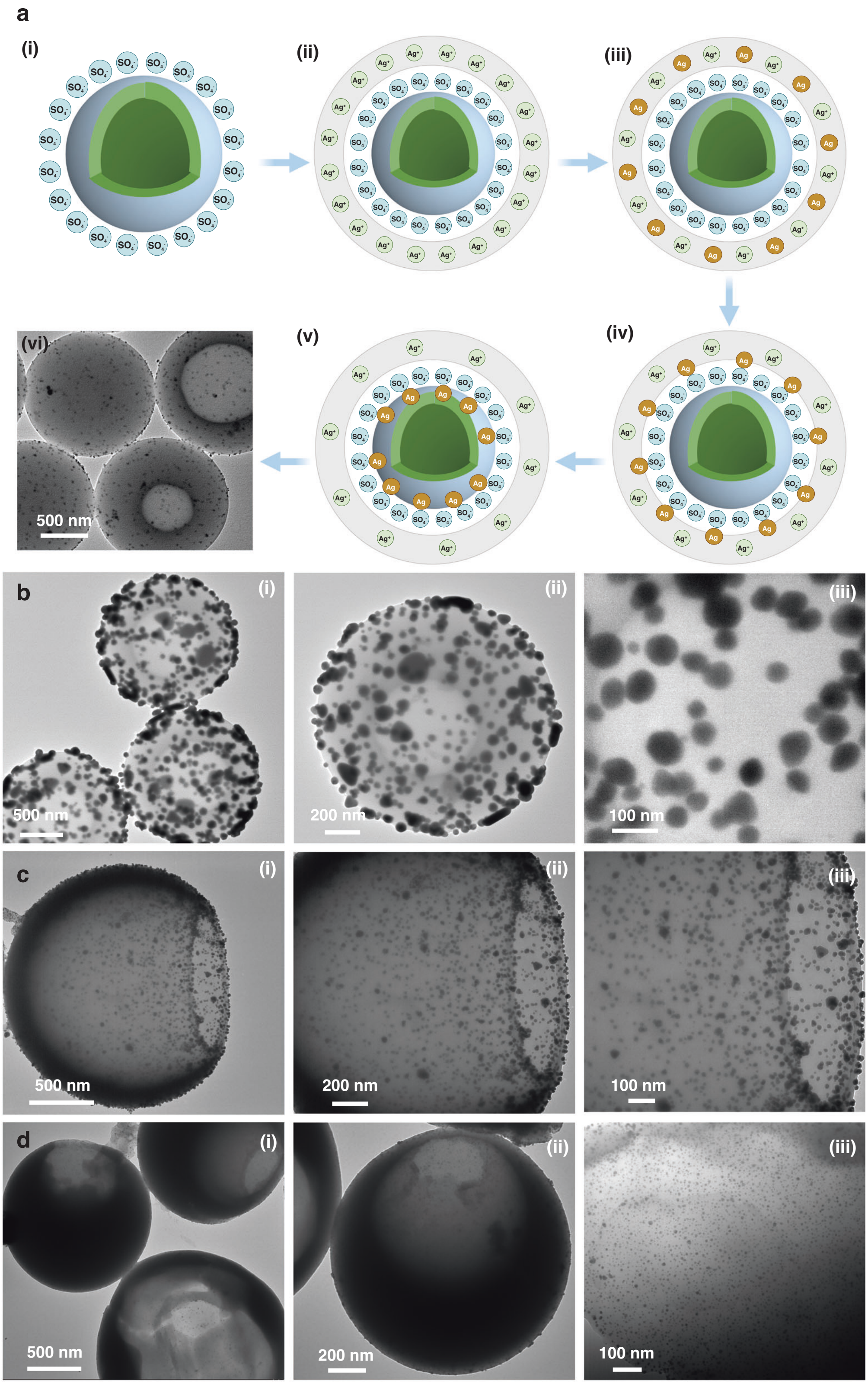

Fig. 5 The mechanism of the noble metal species is decorating with the hollow polystyrene microspheres and TEM characterizations. **a** The mechanism of Ag-loaded functional hollow polystyrene microspheres synthesis, **b**–**d** the TEM characterization results of the Ag-Au, Ag, Ag-Pt loaded PS microspheres at different magnifications

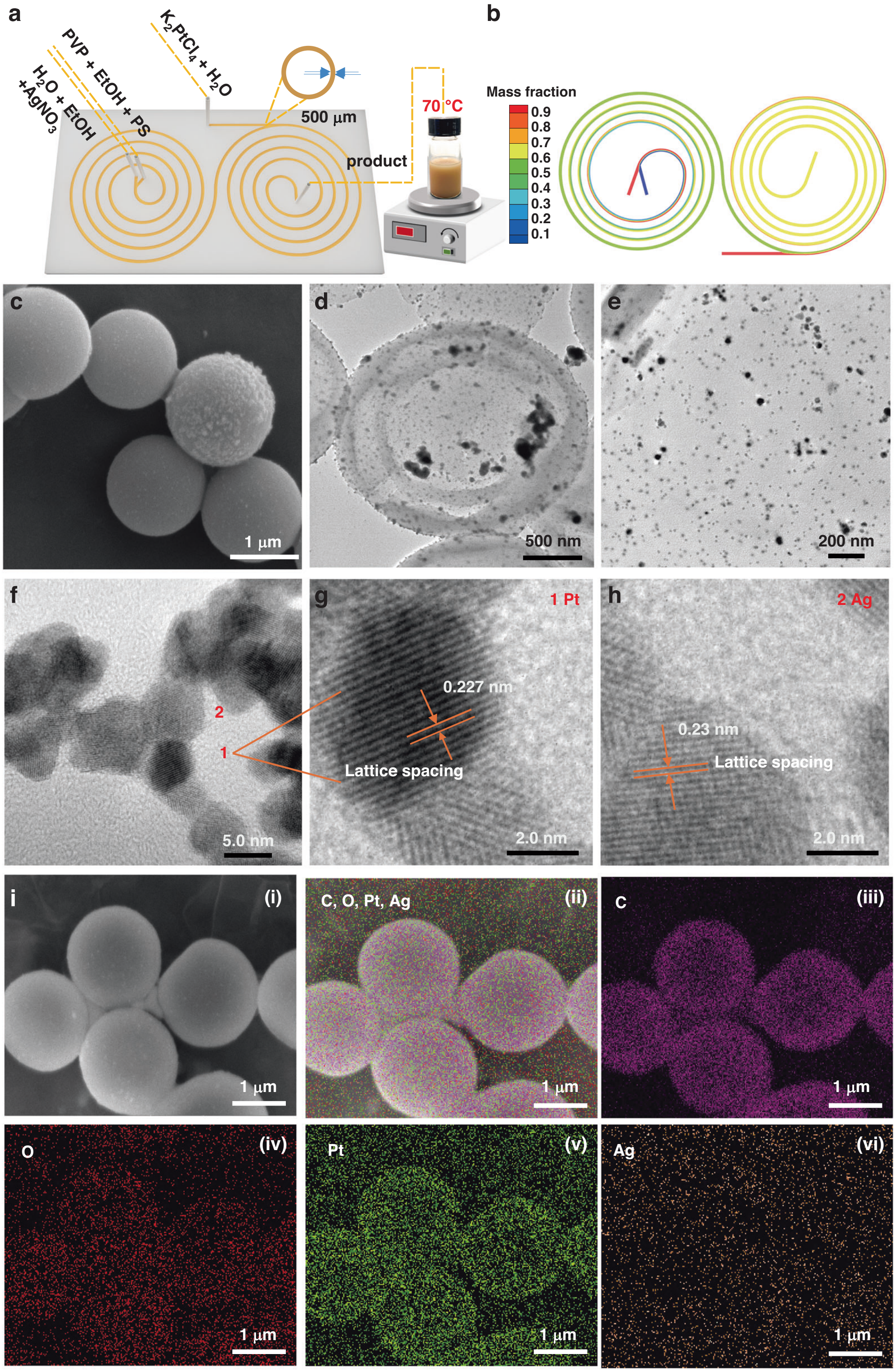

Fig. 6 Continuous flow synthesis of Ag-Pt@HPS microspheres in a spiral microreactor. **a** the schematic diagram and the geometrical parameters of the spiral microreactor, **b** the simulation results of the mixing performance in the spiral microreactor, **c** SEM image of the Ag-Pt@HPS microsphere fabricated in the microreactor, **d** TEM image of the Ag-Pt@HPS microsphere, **e** the TEM image of Pt and Ag nanoparticles distribution on the PS microsphere, **f**–**h** the fringe lattices of the Pt and Ag nanoparticles with HRTEM characterization, **i** EDS mapping image area(i), and EDS mapping results of the Ag-Pt@HPS microspheres

controlled PS microspheres. The mixing performance in the spiral microreactor was also validated by the numerical simulation as demonstrated in Fig. 6b, the results revealed that the mixing could be rapidly finished in the third cycle of the developed spiral microchannel even with three fluids pumped into the microchannel. The formation mechanism is similar with the monometallic Ag nanoparticles loading process. It was found that when the $AgNO_3$ ethanol-water mixture and K_2PtCl_4 aqueous solution were introduced into the spiral microchannel simultaneously and maintain the flow rates of three inlets were 30 μL/min, the color of product suspension gradually changed from white to light brown, the final color of the product depicted in Fig. S4b. The SEM image of Ag-Pt@PS was illustrated in Fig. 6c, indicating that the fabricated Ag-Pt@PS microspheres possessed good spherical morphology and monodisperse. The TEM images at different magnifications were displayed in Fig. 6d, e. Figure 6d revealed that Ag-Pt@PS microspheres exhibited a hollow structure. Additionally, Ag and Pt nanoparticles were distributed uniformly on the surface of the hollow PS microspheres as demonstrated in Fig. 6e. The HRTEM images (Fig. 6f) were captured to determine the fringe lattice of the Pt and Ag nanoparticles, and the fringe lattice of the Pt and Ag nanoparticles were 0.227 and 0.23 nm, respectively (Fig. 6g, h), and the measurements process via open software digital micrography were attached to Fig. S5. The EDS mapping results revealed that the element distribution on the hollow PS microspheres was illustrated in Fig. 6i. It was clear that the Ag and Pt nanoparticles were successfully loaded on the hollow PS microspheres. It was worth noting that the whole fabrication process could be completed within 15 min owing to the remarkable mixing efficiency, short mass transfer distance and confined effect, which is not possible with conventional synthetic technology. More importantly, the fast formation of the Ag@PS at the microscale allowed us to prepare the co-catalyst on a large scale by adopting a continuous flow microreactor system.

For bimetallic Au and Ag nanoparticles immobilized PS microsphere preparation, readily change the K_2PtCl_4 to $HAuCl_4$ aqueous solution. The synthetic procedures of the Ag-Au@PS were displayed in Fig. 7a, b. The SEM images at different magnifications indicated that there are considerable amounts of nanoparticles embedded on the PS microspheres, and those functionalized PS microspheres exhibited good sphericity and monodisperse (Fig. 7i–k). The TEM images at different magnifications revealed that the prepared Ag-Au@PS microspheres have a hollow structure, which is beneficial for Ag and Au nanoparticles anchoring (Fig. 7c–e) and the fabricated nanoparticles are evenly distributed on the surface of hollow PS microspheres. HRTEM images were captured to measure the fringe lattice of the Au nanoparticles (Fig. 7f). Figure 7g showed the fast fourier transform image obtained from open software digital micrography to determine the fringe lattice of the Au nanoparticles, and the results confirmed that the fringe lattice of the Au nanoparticles was 0.258 nm (Fig. 7h). Figure 7l clarified that the EDS mapping results, which further prove that the Au and Ag elements were uniformly distributed on the hollow PS microsphere and the Au and Ag nanoparticles were successfully embedded on the hollow PS microspheres. Compared to the bimetallic Ag and Pt nanoparticles on the hollow PS microspheres (Fig. 6c), it was evident that the size of Au nanoparticles was larger than the Pt nanoparticles (Fig. 7i–k). To investigate the effect of the morphology of the catalyst carrier on the follow-up catalytic performance, we functionalize the versatile nanoparticles on the morphology-varied PS microspheres, the modification process was similar to that of Ag@PS, Ag-Pt@PS, and Ag-Au@PS. The detailed procedures and characterization results were provided in Figs. S6–S8. Additionally, the X-ray photoelectron spectroscopy (XPS) was employed to verify the decoration of the noble metal species and corresponding oxidation states in Ag-Au@OHPS and Ag-Pt@OHPS. The results revealed that the high resolution of Ag3d spectrum displays two characteristic peaks at 374.3 and 368.3 eV, demonstrating that Ag^0 is the active species for the reaction (Figs. S7i and S8i). For Au species in Ag-Au@OHPS, the high resolution of Au4f spectrum exhibited two feature peaks at 87.9 eV and 84.3 eV, proving the Au exists in Au^0 (Fig. S7j). For Pt species in Ag-Pt@OHPS, Pt 4 f spectrum displays two characteristic peaks, namely Pt4f $_{5/2}$, and $Pt4f_{7/2}$, respectively, and the corresponding binding energy are positioned at 74.6 eV and 71.1 eV, hinting that Pt exists in Pt^0 (Fig. S8j), these metallic state exhibits higher catalytic activity and were conducive to promote the catalytic performance.

The catalytic performance studies

The produced Ag, Ag-Au, and Ag-Pt loading PS, hollow, and open hole PS microspheres were used as a catalyst to evaluate their catalytic performance in the 4-NP catalytic reduction reaction into 4-AP in the presence of $NaBH_4$. The representative catalytic models were demonstrated in Fig. 8a. The ultraviolet absorption spectrum of the 4-NP, $4\text{-}NP^+$, and 4-AP were displayed in Fig. 8c. At the beginning, the 4-NP solution exhibited a yellow color but converted into yellow-green once the $NaBH_4$ was introduced into the system, and the color gradually converted into colorless when the Ag@OHPS was added into the mixture, as displayed in Fig. 8b. It was evident that when the Ag-OHPS was introduced into the 4-NP solution in the presence of reduction agent $NaBH_4$, an apparent peak occurred when the reaction time reached 6 min (Fig. 8d), which demonstrated that a new product 4-AP was formed in the system. When the Ag-

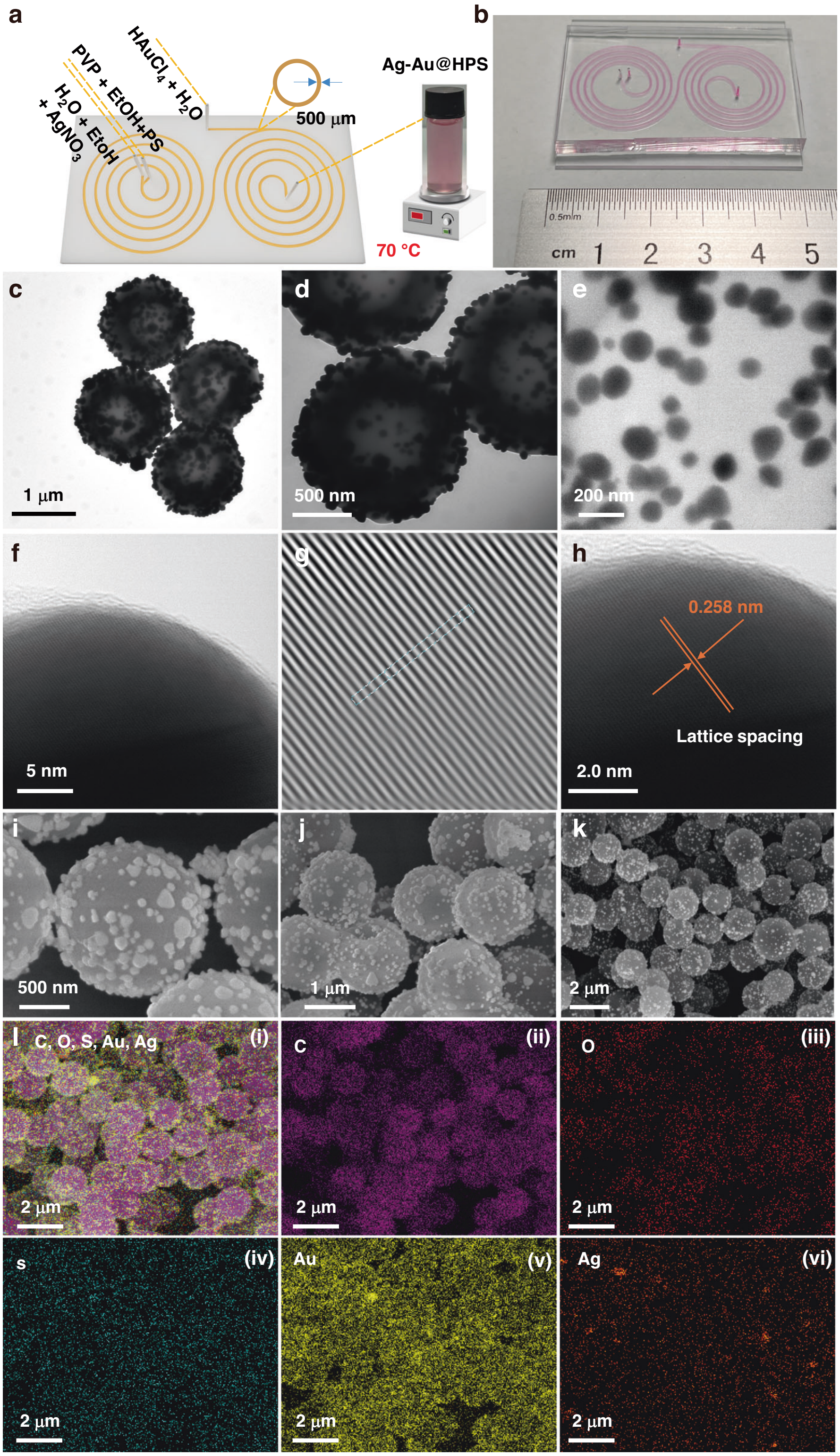

Fig. 7 Continuous flow synthesis of Ag-Au@HPS microspheres in a spiral microreactor. **a** the schematic diagram and the geometrical parameters of the spiral microreactor, **b** the physical diagram of the PDMS spiral microreactor, **c** SEM image of the Ag-Au@HPS microsphere fabricated in the microreactor, **d** TEM image of the Ag-Au@HPS microsphere, **e** the TEM image of Ag and Au nanoparticles distribution on the PS microsphere, **f**–**h** the fringe lattices of the Ag and Au nanoparticles with HRTEM characterization, **i**–**k** SEM images of Ag-Au@HPS microspheres at different magnifications, **l** EDS mapping images of Ag-Au@HPS microspheres

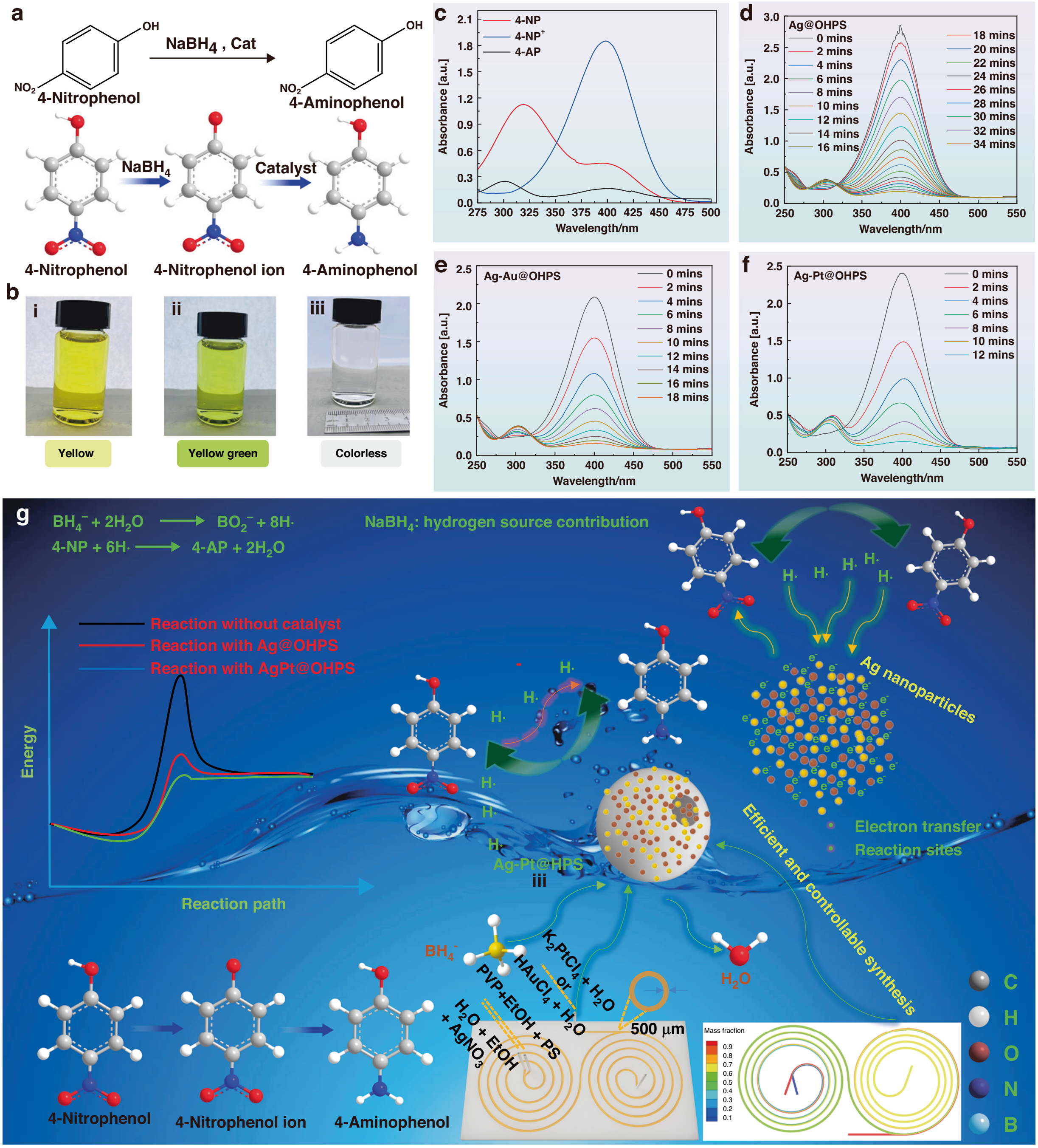

Fig. 8 The catalytic performance of the Ag-loaded hollow PS microspheres for 4-NP reduction into 4-AP. a the chemical reduction reaction equation of the 4-NP into 4-AP in the presence of $NaBH_4$ and catalyst, **b** the color change during the reaction process, **c** the UV–vis spectrum of the 4-NP, 4-NP$^+$, and 4-AP, **d** The UV–vis spectrum variation process in the process of the reaction with Ag@OHPS, **e** The UV–vis spectrum variation with Ag-Au@OHPS as catalyst, **f** The UV–vis spectrum variation with Ag-Pt@OHPS as catalyst, **g** The catalytic mechanism of the 4-NP reduction into 4-AP in the presence of the catalyst

Au@OHPS and Ag-Pt@OHPS served as catalysts and were introduced into the 4-NP reaction medium in the presence of $NaBH_4$, the 4-AP feature peak occurred at 4 and 2 min, respectively, as displayed in Fig. 8e, f. Then, the peak intensity of the 4-NP$^+$ decreased significantly as the reaction time increased, indicating that the 4-NP$^+$ in the reaction system was consumed continuously. It was obvious that the reactant was completely consumed and 4-NP was converted into 4-AP within approximately 34, 18, and 12 min at about 0 °C in the presence of

Ag@OHPS, Ag-Au@OHPS, and Ag-Pt@OHPS PS microspheres, which indicated superior catalytic reduction performance of Ag-loaded open hole PS microspheres. The excellent catalytic performance is attributed to two factors: on the one hand, the large surface area of the hollow structure, which facilitated the absorption of the 4-NP, BH_4^-, and accelerated the diffusion of the reactant into the surface of the Ag/Pt nanoparticles; on the other hand, the specific hollow structure of the PS microsphere effectively captured the Ag and Pt nanoparticles, promoting the mass transfer and further executed the chemical reaction efficiently. The catalytic mechanism with noble metal nanoparticles decorated morphology-controlled PS microspheres could be explained as follows: in the aqueous environment, $NaBH_4$ dissociates into Na^+ and BH_4^- rapidly. BH_4^- was further hydrolyzed to produce reactive hydrogen species and participated in the reaction as reducing agents, the hydrogen active species from BH_4^- decomposition transferred electrons to the surface of Ag/Pt nanoparticles, and Ag/Pt served as a conducting medium to transfer the electrons to the absorbed 4-NP to complete the reduction reaction gradually, as illustrated in Fig. 8g.

In this catalytic reaction validation model, the concentration of $NaBH_4$ is much higher than the concentration of the catalyst, therefore, the catalytic reduction reaction was assumed to follow the first-order reaction kinetics. Therefore, the catalytic reaction kinetic equation can be expressed in Eq. (3).

$$kt = \ln \frac{C_t}{C_0} = -\ln \frac{A_t}{A_0} \tag{3}$$

Where k is the apparent rate constant (s^{-1}), t is the catalytic reaction time (min), C_0 and C_t are the concentration of the 4-NP^+ when the reaction time was 0, and t, respectively. A_0 and A_t were the violet-visible absorption peak values of the 4-NP^+ at the reaction times were 0 and t. The reaction kinetics curve of 4-NP was illustrated in Fig. 9, the fitting results were well fit to the first-order reaction kinetics with different amounts of catalyst and catalytic carriers. As displayed in Fig. 9, the effect of the morphologies of the catalyst carrier, types of the noble metal nanoparticles, amount of the catalyst were investigated comprehensively. As illustrated in Fig. 9a, for monometallic noble metal loaded PS microspheres with varied morphologies as catalyst, fixed 0.005 mg catalyst, it was evident that the morphology of the catalyst carrier exhibited a significant effect on the reaction kinetics constant, and the catalytic performance of Ag@OHPS catalyst outperforms the Ag@PS and Ag@HPS. At the same operation conditions, the reaction rate constant was 6×10^{-4} s^{-1}, 9×10^{-4} s^{-1}, and 1.4×10^{-3} s^{-1}, respectively, which is attributed to the large surface area of the hollow and open hollow structure of the PS microspheres. As demonstrated in Fig. 9b, c, for bimetallic Ag-Pt and Ag-Au nanoparticles functionalized PS microspheres, the results revealed that the morphologies of the catalyst carrier exhibit negligible effect with Ag@Pt loaded PS microspheres as catalyst, on the contrary, the morphology of the catalyst carrier displayed great impact on reaction performance with bimetallic Ag-Au species decorated on the morphology-controlled PS microspheres, the reaction rate constant were 1.09×10^{-3} s^{-1}, 1.97×10^{-3} s^{-1}, and 2.43×10^{-3} s^{-1}, respectively with Ag-Au@PS, Ag-Au@HPS, and Ag-Au@OHPS served as catalyst, this phenomenon was similar with the monometallic noble Ag nanoparticles loaded PS microspheres with different morphologies. The remarkable surface of the catalyst carrier contributes to anchoring considerable noble nanoparticles and further provides more accessible reaction sites. Additionally, compared to the PS and HPS substrate, the single open hole on the OHPS microspheres not only provides the confined micro-environment for efficient mass transfer and electron transfer but also offers abundant reaction active sites, which result in rapid reaction kinetics. In summary, both the large surface area, abundant accessible active sites and confined space simultaneously promoting the catalytic reduction reaction, therefore, the reaction rate and catalytic activity were enhanced significantly with bimetallic species decorated OHPS as catalyst, and the value of the first-order reaction constant and catalytic activity were much larger than the previously reported. Fixed the morphology of the catalyst carrier as PS, hollow PS, and open hollow PS microspheres (Fig. 9d–f), the effect of the noble metal nanoparticles was studied, the results indicated that bimetallic noble nanoparticles shown much superior catalytic performance than the monometallic noble metal nanoparticles loaded on the morphology-controlled PS microspheres owing to adjustable electronic and surface stains effect of bimetallic nanoparticles[25], another reason is that bimetallic nanoparticles synergistically enhance the catalytic activity and accelerate the reaction. Among bimetallic noble nanoparticles modified PS microspheres, it is obvious that Ag-Pt@OHPS displayed the most outstanding catalytic performance. The high catalytic performance with Ag-Pt@OHPS could be explained as follows: compared to the Au, Pt species could serve as powerful hydrogen source and could generate active hydrogen species. The produced hydrogen species rapidly migrate to the Ag or the interface of Ag-Pt active sites by “spillover”, which significantly enhance the concentration of the hydrogen species on the surface nanoparticles and promote the reaction activity. On the contrast, the Ag nanoparticles have superior adsorption ability to the 4-NP. The co-effect of the Pt and Ag nanoparticle’s synergistic catalyzes the 4-NP reduction

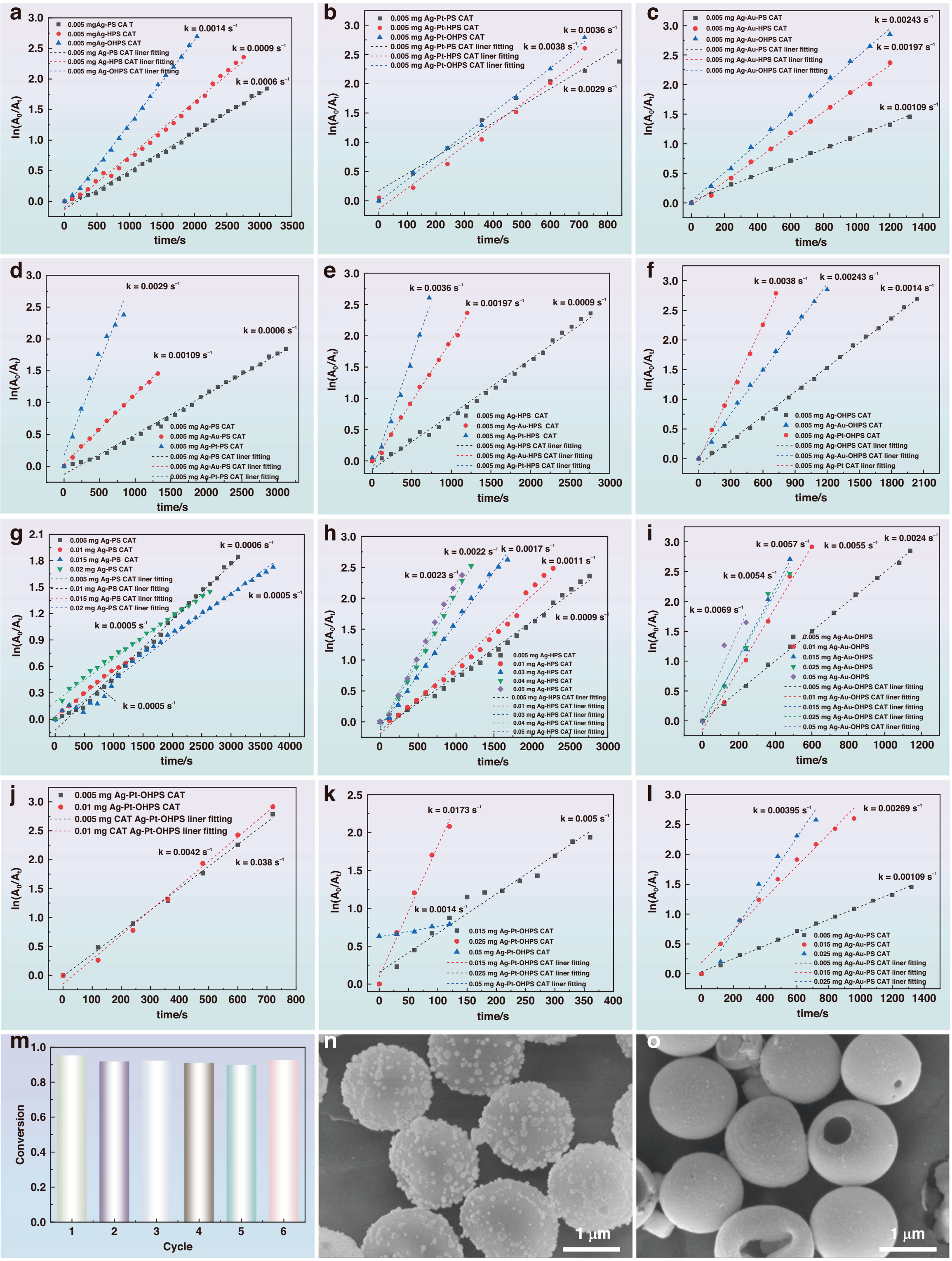

Fig. 9 The pseudo first-order reaction kinetics fitting results and recyclability test of PS microspheres with different catalytic carrier morphologies and various noble metal nanoparticles as catalysts. a–**f** The first-order reaction kinetics fitting results with different noble metal nanoparticles modified PS microspheres with versatile morphologies, **g**–**l** The first-order reaction kinetics fitting results with varied amounts of catalyst, **m** the recyclability of the Ag-Pt@OHPS microsphere, **n** the SEM image of Ag-Au@OHPS microspheres after 5 cycles, **o** the SEM image of the Ag-Pt@OHPS microspheres after 5 cycles)

into 4-AP efficiently. Different amounts of catalyst were added to the reaction system to further investigate the catalytic performance. The results revealed that the amount of catalyst possesses a negligible effect on catalytic performance, with Ag nanoparticles loaded with PS microspheres serving as the catalyst. Increasing the catalyst amount from 0.005 to 0.02 mg, the corresponding reaction rate remains constant with a value of $5 \times 10^{-4}\,s^{-1}$ (Fig. 9g). For Ag@HPS, the pseudo first-order fitting results revealed that the reaction rate constant increased from 0.005 mg to 0.05 mg as the amount of the catalyst increased from $9 \times 10^{-4}\,s^{-1}$ to $2.3 \times 10^{-3}\,s^{-1}$ (Fig. 9h). Additionally, we found that the increase in degree became small when the catalyst amount increased to 0.04 mg, which may be affected by diffusion rather than mass transfer. For bimetallic Ag-Au@OHPS, the catalytic results indicated that the reaction rate constant increased from $2.4 \times 10^{-3}\,s^{-1}$ to $6.9 \times 10^{-3}\,s^{-1}$ (Fig. 9i). For Ag-Pt@OHPS and Ag-Au@PS catalysts (Fig. 9j–l), the results exhibited similar trends. One notable difference was that when the Ag-Pt@OHPS increased to 0.025 mg, the reaction rate constant decreased dramatically (from $1.73 \times 10^{-2}\,s^{-1}$ to $1.4 \times 10^{-3}\,s^{-1}$) with a continuous increase in Ag-Pt@OHPS to 0.05 mg, owing to the mass transfer being limited, whereas the diffusion became the dominant factor. These findings revealed that whether monometallic or bimetallic, the reaction rate constants increased significantly with the catalyst amount within a certain range. The chemical reaction rate constant corresponding to units of various catalysts was summarized in Table S2. The comparison results revealed that the catalyst in this study outperforms the published literature[9] as demonstrated in Table S3. The catalyst exhibited rapid chemical reaction kinetics, superior catalytic activity at a low concentration of the catalyst for the reduction of 4-NP in contaminated wastewater and promising degradation of other environmental pollutants.

Eventually, the recyclability of the Ag-Pt@OHPS was tested to evaluate the life of the catalyst, it was obvious that the reaction activity was maintained well without the sacrifice of the catalytic activity and efficiency even after 5 cycles, as shown in Fig. 9m, which suggests that both the noble metal nanoparticles loaded PS microspheres were robust under the catalytic conditions and facilitates to reuse for future practical applications. The recyclability performance was evaluated by the conversion of the 4-NP, and the conversion rate X was defined as in Eq. (4).

$$X = \frac{C_0 - C_t}{C_0} = 1 - \frac{C_t}{C_0} \tag{4}$$

Here, C_0 and C_t were the concentration of the 4-NP at the initial and final reaction, the SEM images of the Ag-Au@OHPS and Ag-Pt@OHPS catalysts after 5 cycles of use were displayed in Fig. 9n, o. The SEM images of other recycled catalysts were also provided in Fig. S9, and the ICP characterization results of the catalyst before and post reaction were provided in Tables S4 and S5.

Conclusions

In this study, an efficient and facile strategy was developed to fabricate the morphology-controlled hollow PS microsphere and a continuous flow synthetic strategy to prepare Ag, Ag-Au, Ag-Pt loaded PS, HPS, and OHPS, respectively, in a spiral microreactor for practical synergistic catalysis applications. The effect of the composition of the water-ethanol and aging time in the water-ethanol mixture was investigated systematically. Hollow, dimple-, bowl-like hollow PS microspheres were successfully fabricated in the water-ethanol binary mixture. Tiny toluene was introduced in the water-ethanol mixture, with dimple-like PS microspheres serving as seeds to prepare open-hole PS microspheres. The morphology and evolution behavior of the PS microsphere were monitored by the SEM and TEM, and the formation mechanism was proposed to explain the morphology evolution phenomenon. A spiral microchannel was developed to immobilize noble monometallic and bimetallic nanoparticles on the PS microspheres successfully in minutes, and the embedding mechanism was also developed to clarify how the noble metal was modified on the PS microspheres. The catalytic performance of the various catalysts was measured by catalyzing the 4-NP reduction into 4-AP, and the effects of the PS morphologies and the types of noble metal nanoparticles were experimentally studied. The results revealed that the catalytic reduction reaction kinetics were well fitted to the first-order kinetics, and open hole PS microspheres loaded with bimetallic Ag-Pt nanoparticles exhibited the best catalytic performance, with a reaction rate constant was $1.73 \times 10^{-2}\,s^{-1}$ and activity parameter was $692\,s^{-1} \cdot g^{-1}$. More importantly, the cycle numbers of the Ag-Pt@OHPS reached up to 5 times without sacrificing catalytic activity, which suggests that the Ag-Pt@OHPS microspheres possess outstanding stability and reusability. In summary, this work not only develops an efficient and facile strategy to produce noble monometallic and bimetallic nanoparticles supporting multifunctional catalytic microspheres in a continuous way but also provides new insights for other various supported noble metallic nanoparticles co-catalyst preparation for confined and synergistic catalytic applications.

Experimental section

Chemicals and reagents

Polyvinylpyrrolidone (average molecular weight is 58000, K29-32) was purchased from Shanghai Macklin Biochemical Technology Co. Ltd, anhydrous ethanol was obtained from Tianjin KeMao Co. LTD, styrene (CP, containing 10–15 ppm 4-tert-butylcatechol stabilizer), ammonium persulfate (APS, 99.99%, ammonium persulfate), and 4-nitrophenol (99%, contains ~3% water) were purchased from Aladdin Co. LTD, toluene (analytical reagent, 99.5%) was bought from Sinopharm Chemical Reagent Co. Ltd, Silver nitrate ($AgNO_3$, 99.8%) was purchased from Sinopharm Chemical Reagent Co. Ltd; K_2PtCl_4, $HAuCl_4$, and sodium borohydride ($NaBH_4$) were obtained from Macklin, and fresh deionized water made in the laboratory was utilized throughout the entire experiment. All the materials used in the experiment were without additional purification.

Synthesis of the hollow PS microsphere with well-defined morphology

The $0.9 \times g$ polystyrene microsphere seeds fabricated via dispersion polymerization (Note S2 and Fig. S10) were dispersed in a water-ethanol mixture with 2 min sonication under 250 W output power, and then the milky white emulsion was placed in the magnetic stirrer at 70 °C with 400 rpm. The sample was collected at different intervals of time (30 min, 1 h, 2 h, 3 h, 4 h, 5 h, 6 h) to monitor the morphology evolution behaviour of the PS microsphere. The swelling process was quenched in an ice bath, and then the PS microsphere was washed with ethanol three times, with different morphologies collected by centrifugation at 6000 rpm. Finally, the collected PS microsphere was moved to the vacuum drying oven (−0.1 MPa, Shanghai Scientific Instrument Co. Ltd), and the dry temperature was 45 °C to evaporate the ethanol to obtain the dry PS microsphere. For the single open hole hollow PS microspheres fabrication, 0.55 mL toluene was introduced into the 5.5 mL aqueous solution (involving $0.02 \sim 0.2 \times g$ PS microspheres) to facilitate PS microspheres swelling, followed by evaporating the solvent at room temperature to obtain the open hole PS microspheres for catalytic applications.

Fabrication of the spiral microchannel

The film mask pattern of the spiral microchannel was designed by AutoCAD 2025. Specifically, the width and the depth of the main spiral microchannel are 500 and 80 μm, respectively, the overall length of the single spiral microchannel is 110 mm. The mold of the spiral microchannel was fabricated by standard photolithography procedures. Following this by pouring the PDMS precursor (Sylgard 184 kit, Dow Corning, 10:1 w/w ratio of base to curing agent) into the mold to generate the PDMS microchannel. Next, the mold was put into the oven at 65 °C for 3 h to dry, and the microchannel was cured and peeled from the mold. Then, the spiral microchannel was punched to generate inlets, outlets, and a main microchannel. Finally, the microchannel was sealed onto a glass slide via the oxygen plasma treatment of the surface of the microchannel. The detailed fabrication procedures of the spiral microchannel were displayed in Fig. S11.

Numerical simulation

The numerical simulation was conducted to validate the mixing performance of the designed spiral microchannel. The commercial software Fluent was employed to execute numerical simulations. The water and ethanol were served as inlet fluids; the density and viscosity of the water were 998.2 kg/m^3, and 0.001 Pa·s, respectively; the density and viscosity of the ethanol were 790 kg/m^3, and 0.0012 Pa·s, respectively. The diffusion coefficient of the mixture was set to 9.85×10^{-10} m^2/s. The flow rates of the two or three inlets were set as 30 μL/min, and the flow pattern was regarded as laminar. In this situation, the flow within the spiral microchannel was steady-state, incompressible. The governing equations were expressed as follows[48]:

$$\nabla \cdot (\rho U) = 0 \tag{5}$$

$$\rho U \cdot \nabla U = -\nabla P + \mu \Delta U \tag{6}$$

$$\rho U \cdot \nabla \mathrm{Y_i} = \nabla \cdot (\rho D \nabla \mathrm{Y_i}) \tag{7}$$

Where ρ and μ were the density and dynamical viscosity of the fluids, D was the mass diffusion coefficient of species, $\mathrm{Y_i}$ was tand he mass transfer of the species i. The boundary condition of the microchannel wall was defined as follows: the inlets and outlets were set as velocity and pressure, respectively; moreover, the boundary condition was regarded as no-slip. The second-order upwind methods were employed to discretize, and the SIMPLE solver was utilized to solve the equation; the convergence residuals were set as 10^{-9}.

Continuous flow synthesis Ag nanoparticles embedded in PS microspheres in a spiral microchannel

Hollow PS microspheres loaded with Ag and bimetallic nanoparticles were fabricated by in situ reduction reaction in a continuous flow spiral microchannel, which omits the complicated pre-prepared synthetic Ag nanocrystals and surface pre-treatment procedures. In brief, 0.02 vacuum-dried PS microspheres were dissolved in 3 mL of ethanol, serving as one phase. $0.03 \times g$ of $AgNO_3$ and $0.003 \times g$ of PVP were added to the water-ethanol mixture (1 mL DI water and 2 mL ethanol), serving as another phase. Following, two-phase fluids were sonicated to allow complete mixing. Then, the two-phase fluids were pumped into the inlets of the spiral microchannel with flow rates were 30 μL/min to allow complete mixing and convert $AgNO_3$ into the Ag nanoparticles; the products were collected in a vial and placed in a 60 °C water bath with a magnetic bar stirring at 400 rpm to enable the reaction to complete. Finally, the collected samples were placed in an ice bath to quench the reaction, followed by the dark yellow reaction mixture being centrifuged at 8000 rpm and washed with fresh DI water three times. Ultimately, the resulting Ag-loaded PS microspheres with various morphologies were dispersed in water for subsequent catalytic application. The detailed process to prepare the Ag-loaded hollow PS microsphere in the batch reactor is illustrated in Fig. S12.

Continuous flow synthesis of bimetallic nanoparticles loaded PS microspheres in a spiral microchannel

For bimetallic immobilizing functional Ag-Pt PS microsphere preparation, $0.03 \times g$ $AgNO_3$ and 0.003 g PVP were dissolved in 0.5 mL water and mixed with 1.5 mL ethanol, serving as one phase; 0.5 mL K_2PtCl_4 (1 mM) aqueous solution was mixed with 1.5 mL ethanol, serving as another phase whereas $0.02 \times g$ dry PS microsphere dispersed in 2 mL ethanol was the third phase. Three-phase fluids were pumped into three inlets of the spiral microchannel by high-pressure syringe pumps with flow rates were 30 μL/min to facilitate complete mixing and reaction in the microchannel. The process for Ag/Au embedding PS microspheres production was the same as for Ag-Au loading PS microspheres preparation, except for replacing K_2PtCl_4 with $HAuCl_4$.

The catalytic reaction model validation

The catalytic reduction reaction of 4-NP to 4-AP in the presence of $NaBH_4$ is proposed as a catalytic reaction model to characterize the catalytic activity of Ag-loaded PS and hollow PS microspheres at the microscale. A fresh $NaBH_4$ aqueous solution (0.2 M) and 4-nitrophenol aqueous solution (5.0 mM) are prepared with 4 °C ice water. All the pre-prepared solutions were stored in the ice bath. 0.1 mL of 4-NP aqueous solution and 1 mL of $NaBH_4$ aqueous solution were added to the quartz cuvette and then diluted to 3.7 mL with ice-deionized water. Finally, a certain volume of catalyst (0.5 mg/mL) of Ag, Ag-Au, and Ag-Pt loaded PS microspheres was respectively pipetted into the mixture, and then the ultraviolet–visible (UV–Vis) absorption spectra were recorded to monitor the reaction process in real-time.

Characterization and measurements

The Fourier Transform Infrared (FTIR) Spectrometer (Thermo Fisher Scientific Nicolet iS20, American) was utilized to characterize the group on the surface of the PS microsphere, and the Zetasizer Nano ZSE (Malvern, UK) was used to analyze the potential of the PS seed microsphere. The morphology and size of the PS microsphere were characterized by field emission scanning electron microscopy (SEM, MAIA3 LMH, TESCAN, Czech) at a voltage of 10 kV. The size and size distribution were analyzed using the open-source software ImageJ. TEM with a voltage of 100 kV (TEM, Ruli, HT7800) was adopted to observe the Ag nanoparticles on the interior and external surfaces of the hollow, patchy, and dimple PS microspheres. HRTEM (JEOL JEM-2100Plus) was utilized to observe the fringe lattice of the Ag, Au, and Pt nanoparticles. ICP-OES/MS (Agilent 5110 (OES), American) was used to determine the mass loading of the Ag nanocrystals on the PS microsphere. XPS (Thermo Scientific K-Alpha) instrument equipped with a monochromated Al Kα radiation (1486.6 eV) was employed to verify the oxidation state of the noble metal species. UV–Vis absorption spectrums were collected by the ultraviolet–visible spectrophotometer (UV1600).

Acknowledgements
This work was supported by the National Key R&D Program of China (2023YFC3904301), the Key R&D Program of Shaanxi Province (2024GX-YBXM-471), the Qin Chuang Yuan Talent Program (2021QCYRC4-33), and the Distinguished Overseas Young Scholars of the National Natural Science Foundation of China (GYKP032).

Author details
[1]School of Chemical Engineering and Technology, Xi'an Jiaotong University, Xi'an 710049 Shaanxi, P.R. China. [2]Key Laboratory of Education Ministry for Modern Design and Rotor-Bearing System, School of Mechanical Engineering, Xi'an Jiaotong University, Xi'an 710049 Shaanxi, P.R. China. [3]Nanofluids Technologies Co., Ltd, Xi'an 712000 Shaanxi, P.R. China. [4]State Key Laboratory of Fluorine & Nitrogen Chemicals, School of Chemical Engineering and Technology, Xi'an Jiaotong University, Xi'an 710049 Shaanxi, P.R. China

Author contributions
Li Ma: Conceptualization, methodology, investigation, validation, formal analysis, writing–original draft. Junsheng Hou: Software, simulation, writing–review & editing. Xiong Zhao: Methodology, validation, writing–review & editing. Zijuan Luo: Formal analysis, writing–review & editing. Yilong Yao: Formal analysis, writing–review & editing. Yaxuan Xiao: Formal analysis, methodology, validation. Zihan Ding: Methodology, validation. Zhenzhen Chen: Methodology, validation. Jinjia Wei: Resources, supervision. Nanjing Hao: Funding acquisition, supervision, project administration, resources, writing–review & editing.

Data availability
Data will be made available on request.

Conflict of interest
The authors declare no competing interests.

Supplementary information The online version contains supplementary material available at https://doi.org/10.1038/s41378-026-01176-6.

Received: 29 August 2025 Revised: 26 November 2025 Accepted: 19 December 2025

References
1. Kim, G., Park, K., Zheng, Z. & Jin, S. Size-controllable, single-step, and scalable synthesis of hollow polymer nanoparticles. *Langmuir* **36**, 6202–6209 (2020).
2. Wang, Z. et al. The building of molecularly imprinted single hole hollow particles: a miniemulsion polymerization approach. *Chem. Eng. J.* **357**, 348–357 (2019).
3. Wang, A., Ma, Y. & Zhao, D. Pore engineering of porous materials: effects and applications. *Acs Nano* **18**, 22829–22854 (2024).
4. Dorbic, K. & Lattuada, M. Synthesis of dimpled polymer particles and polymer particles with protrusions – Past, present, and future. *Adv. Colloid Interface Sci.* **320**, 102998 (2023).
5. Hueckel, T. & Sacanna, S. Mix-and-melt colloidal engineering. *ACS Nano* **12**, 3533–3540 (2018).

6. Liu, J., Tan, Z., Qu, X., Liang, F. & Yang, Z. Single-hole janus hollow sphere. *Langmuir* **38**, 11406–11413 (2022).
7. Hyuk Im, S., Jeong, U. & Xia, Y. Polymer hollow particles with controllable holes in their surfaces. *Nat. Mater.* **4**, 671–675 (2005).
8. Hosaka, M., Ichikawa, H., Sajiki, S., Kawamura, T. & Kawai, T. Uniform, convex structuring of polymeric colloids via site-selected swelling. *J. Colloid Inter. Sci.* **659**, 542–549 (2024).
9. Park, S. H., Kim, J., Hur, S. H., Kim, D. H. & Kim, M. H. Heterophase polymer dispersion: a green approach to the synthesis of functional hollow polymer microparticles. *Chem. Eng. J.* **348**, 46–56 (2018).
10. Tian, Q., Yu, X., Zhang, L. & Yu, D. Monodisperse raspberry-like multihollow polymer/Ag nanocomposite microspheres for rapid catalytic degradation of methylene blue. *J. Colloid Inter. Sci.* **491**, 294–304 (2017).
11. Xu, Z., Hueckel, T., Irvine, W. T. M. & Sacanna, S. Caged colloids. *Chem. Mater.* **35**, 6357–6363 (2023).
12. Li, X. et al. Shape-tunable hollow polysiloxane nanoparticles based on a surfactant-free soft templating method and their application as a drug carrier. *Acs Appl. Mater. Inter* **16**, 2672–2682 (2024).
13. Liang, J., Kou, H. & Ding, S. Complex hollow bowl-like nanostructures: synthesis, application, and perspective. *Adv. Funct. Mater.* **31**, 2007801 (2021).
14. Ramli, R. A. Hollow polymer particles: a review. *Rsc Adv.* **7**, 52632–52650 (2017).
15. Fan, Q. et al. Unveiling enhanced electrostatic repulsion in silica nanosphere assembly: formation dynamics of body-centered-cubic colloidal crystals. *J. Am. Chem. Soc.* **145**, 28191–28203 (2023).
16. Fu, Y. et al. Three-dimensional photonic crystal bulks with outstanding mechanical performance assembled by thermoforming-etching cross-linked polymer microspheres. *Acs Appl. Mater. Inter.* **12**, 35311–35317 (2020).
17. Sacanna, S. et al. Shaping colloids for self-assembly. *Nat. Commun.* **4**, 1688 (2013).
18. Zou, H. & Shang, K. Synthetic strategies for hollow particles with open holes on their surfaces. *Mater. Chem. Front.* **5**, 3765–3787 (2021).
19. Sun, X., Huang, Y., Chen, M., Peng, X. & Dou, W. Facile synthesis of single-hole crosslinked particles with embedded single bulge by seeded emulsion polymerization. *Macromol. Chem. Phys.* **219**, 1800150 (2018).
20. Park, S. H., Kim, J., Lee, W.-E., Byun, D.-J. & Kim, M. One-step synthesis of hollow dimpled polystyrene microparticles by dispersion polymerization. *Langmuir* **33**, 2275–2282 (2017).
21. Kim, D. H., Woo, H.-C. & Kim, M. H. Room-temperature synthesis of hollow polymer microparticles with an open hole on the surface and their application. *Langmuir* **35**, 13700–13710 (2019).
22. Wichaita, W., Polpanich, D. & Tangboriboonrat, P. Review on synthesis of colloidal hollow particles and their applications. *Ind. Eng. Chem. Res.* **58**, 20880–20901 (2019).
23. Tian, Q. et al. Multi-hollow polymer microspheres with enclosed surfaces and compartmentalized voids prepared by seeded swelling polymerization method. *J. Colloid Inter. Sci.* **473**, 44–51 (2016).
24. Okubo, M., Kobayashi, H., Huang, C., Miyanaga, E. & Suzuki, T. Water absorption behavior of polystyrene particles prepared by emulsion polymerization with nonionic emulsifiers and innovative easy synthesis of hollow particles. *Langmuir* **33**, 3468–3475 (2017).
25. Jiang, H.-L., Akita, T., Ishida, T., Haruta, M. & Xu, Q. Synergistic catalysis of Au@Ag core−shell nanoparticles stabilized on metal−organic framework. *J. Am. Chem. Soc.* **133**, 1304–1306 (2011).
26. Zhao, Y. et al. Simple surface-assisted formation of palladium nanoparticles on polystyrene microspheres and their application in catalysis. *Inorg. Chem. Front.* **5**, 1133–1138 (2018).
27. Guo, M. et al. Tailoring catalysis of encapsulated platinum nanoparticles by pore wall engineering of covalent organic frameworks. *Angew. Chem. Int. Ed.* **63**, e202410097 (2024).
28. Xu, M. et al. Synergistic growth of nickel and platinum nanoparticles via exsolution and surface reaction. *Nat. Commun.* **15**, 4007 (2024).
29. Liu, N., Zhao, S., Yang, Z. & Liu, B. Patchy templated synthesis of macroporous colloidal hollow spheres and their application as catalytic microreactors. *Acs Appl. Mater. Inter* **11**, 47008–47014 (2019).
30. Liu, Y., Liu, T., Liu, X., Liu, B. & Zhang, M. Highly loaded silver nanoparticle-modified monodispersed polystyrene composite microspheres (PS/Ag) for rapid catalytic reduction of methylene blue. *Polym. Eng. Sci.* **62**, 576–585 (2022).
31. Wu, T. et al. Self-sustainable and recyclable ternary Au@Cu2O–Ag nanocomposites: application in ultrasensitive SERS detection and highly efficient photocatalysis of organic dyes under visible light. *Microsyst. Nanoeng.* **7**, 23 (2021).
32. Hu, T., Zhang, S. & Qi, Y. Unclonable encryption-verification strategy based on bilayer shape memory photonic crystals. *Small* **20**, 2405243 (2024).
33. Xu, H., Liu, B. & Zhang, M. Synthesis of silver nanoparticles composite mesoporous microspheres for synergistic adsorption-catalytic degradation of methylene blue. *Sep. Purif. Technol.* **324**, 124499 (2023).
34. Liu, X., Liu, A., Liu, B. & Zhang, M. Fabrication of monodisperse magnetic polystyrene mesoporous composite microspheres for high-efficiency selective adsorption and rapid separation of cationic dyes in textile industry wastewater. *Langmuir* **40**, 11277–11286 (2024).
35. Huang, X. et al. Continuous production of monodisperse silver nanoparticles suitable for catalysis in a droplet-based microreactor system. *ACS Appl. Nano Mater.* **6**, 8574–8583 (2023).
36. Huang, L. et al. Rational design of 3D-printed microfluidic chips for one-step production of silver nanofluids in thermal management of power electronic chips. *Acs Appl. Mater. Inter* **17**, 23277–23285 (2025).
37. Hao, N., Nie, Y., Xu, Z. & Zhang, J. X. J. Ultrafast microfluidic synthesis of hierarchical triangular silver core-silica shell nanoplatelet toward enhanced cellular internalization. *J. Colloid Inter. Sci.* **542**, 370–378 (2019).
38. Hao, N. et al. Microfluidics-enabled rational design of ZnO micro-/nanoparticles with enhanced photocatalysis, cytotoxicity, and piezoelectric properties. *Chem. Eng. J.* **378**, 122222 (2019).
39. Wu, X. et al. Microfluidic synthesis of multifunctional micro-/nanomaterials from process intensification: structural engineering to high electrochemical energy storage. *Acs Nano* **18**, 20957–20979 (2024).
40. Fan, Y. et al. Effective photodegradation of 4-nitrophenol with CuO nano particles prepared by ionic liquids/water system. *Green. Chem. Eng.* **3**, 15–24 (2022).
41. Jiang, S. et al. A novel strategy to construct supported silver nanocomposite as an ultra-high efficient catalyst. *Appl. Catal. B: Environ.* **283**, 119592 (2021).
42. Yelboğa, M. & Akbayrak, M. Efficient reduction of highly toxic 4-nitrophenol with ultra-low platinum loading on cobalt (II, III) oxide support: facile synthesis and high turnover frequency. *Int. J. Hydrog. Energ.* **102**, 800–815 (2025).
43. Yang, J. et al. Liquid-liquid interfacial approach for rapid synthesis of well-crystalline two-dimensional metal-organic frameworks for nitro reduction. *Chem. Eng. J.* **485**, 149969 (2024).
44. Wang, K. et al. Kinetics of light assisted catalytic reduction of 4-NP over Ag/PDA. *Chem. Eng. Sci.* **259**, 117778 (2022).
45. Alshehri, S. & Shakeel, F. Solubility determination, various solubility parameters and solution thermodynamics of sunitinib malate in some cosolvents, water and various (Transcutol + water) mixtures. *J. Mol. Liq.* **307**, 112970 (2020).
46. Shi, H., Huang, C., Liu, X. & Okubo, M. Role of osmotic pressure for the formation of sub-micrometer-sized, hollow polystyrene particles by heat treatment in aqueous dispersed systems. *Langmuir* **35**, 12150–12157 (2019).
47. Strachan, J., Barnett, C., Masters, A. F. & Maschmeyer, T. 4-nitrophenol reduction: probing the putative mechanism of the model reaction. *ACS Catal.* **10**, 5516–5521 (2020).
48. Hou, J. et al. Microfluidic controllable production and morphology-independent phase-change heat transfer of boehmite nanofluids. *Chem. Eng. J.* **488**, 150605 (2024).